Electronic Supplementary Material (ESI) for Journal of Materials Chemistry A.

Supporting Information for:

Chalcogenide and Pnictide Nanocrystals from the Silylative Deoxygenation of Metal Oxides

Chia-Cheng Lin,[1] Shannon J. Tan[1] and Javier Vela[1,2,*]

[1]Department of Chemistry, Iowa State University, and [2]Ames Laboratory, Ames, Iowa, 50011

Corresponding Author

* vela@iastate.edu

Table S1. Optoelectronic properties of select Ni and Co chalcogenides and pnictides.

Material	Character
NiO	Semiconducting (4.0 eV)[1]
Ni_3S_2	Metallic
Ni_5Se_5	unknown
Ni_2P	Metallic
CoO	Semiconducting (3.4,[i] 4.5 eV[d])[2]
Co_3O_4	Semiconducting (2.13, 3.95 eV)[3]
Co_9S_8	Metallic
Co_9S_8	Metallic
Co_3Se_4	unknown
CoP	Metallic
Co_2P	Metallic
$NiCo_2O_4$	Semiconducting (2.06, 3.63 eV)[4]
$(Ni/Co)_9S_8$	unknown

[i] = indirect, [d] = direct

[1] J.Y. Corey, Chem. Rev. 111 (2011) 863.

[2] C. Rödl, F. Fuchs, J. Furthmüller, F. Bechstedt, Phys. Rev. B 79 (2009) 235114-1.

[3] R. Xu, H.C. Zeng, Langmuir 20 (2004) 9780.

[4] B. Cui, H. Lin, Y.Z. Liu, J.B. Li, P. Sun, X.C. Zhao, C.J. Liu, J. Phys. Chem. C 113 (2009) 14083.

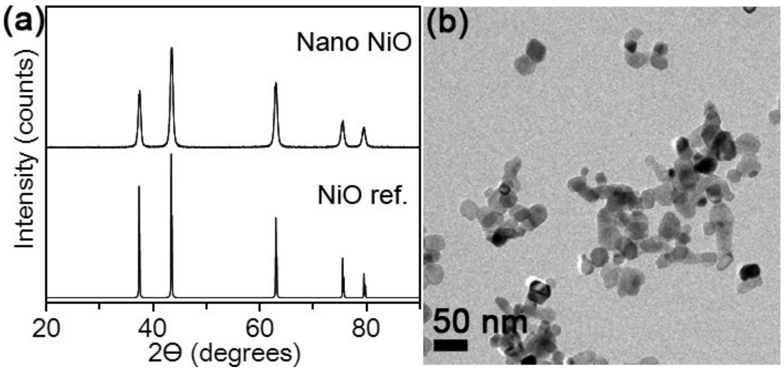

Figure S1. Powder XRD data for NiO nanocrystals (Scherrer: 14.1±0.4 nm), bulk NiO reference (a) and representative TEM image of NiO nanocrystals (18±4 nm) (b).

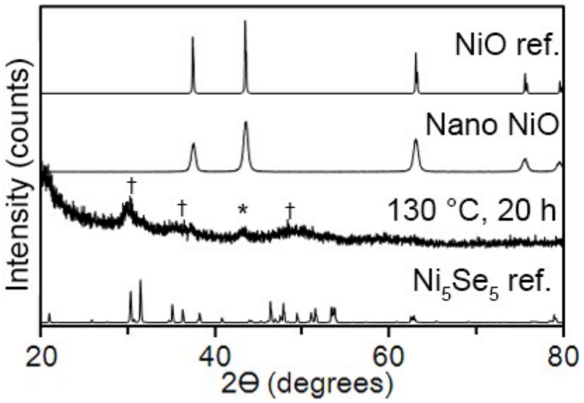

Figure S2. Powder XRD patterns of NiO nanocrystals and their silylative deoxygenation product upon reaction with TMS_2Se. Reported XRD patterns for bulk rock salt NiO(*) and Ni_5Se_5 ($) are shown for comparison.

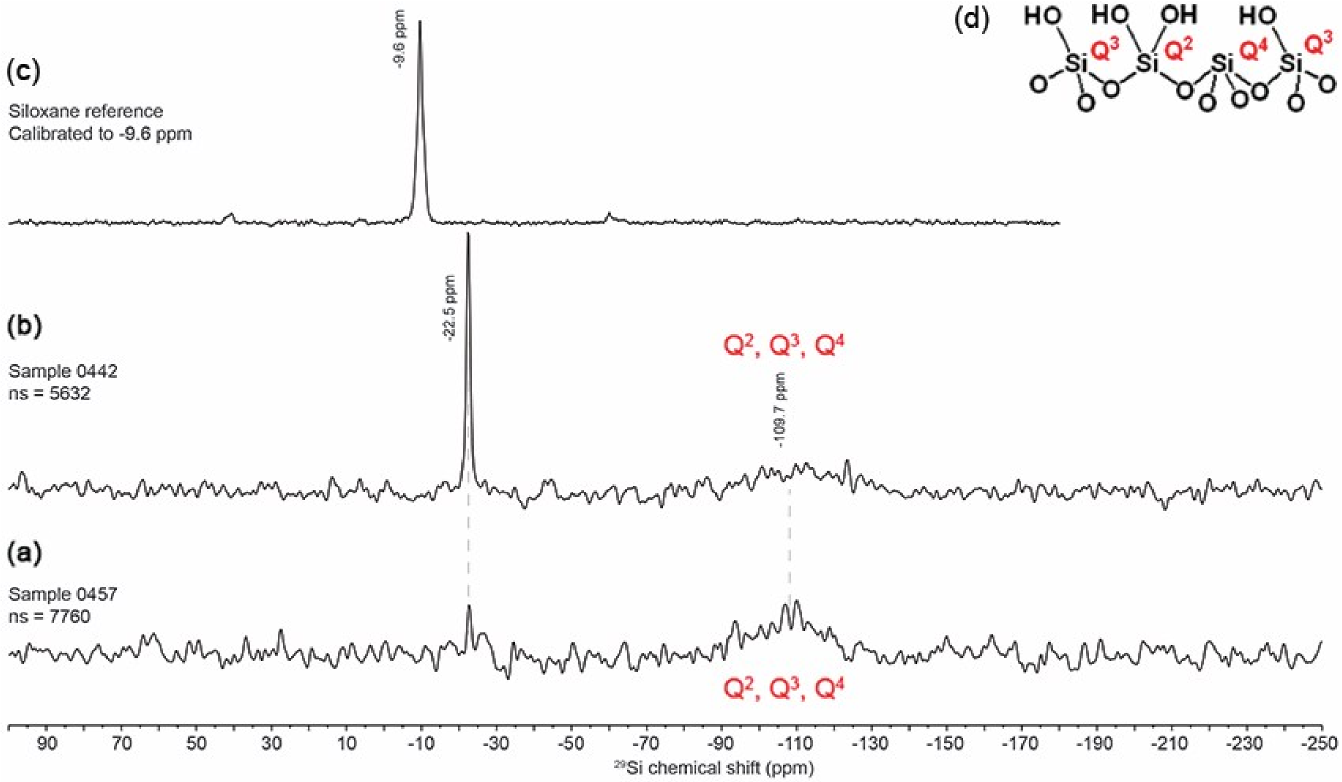

Figure S3. DP-MAS ^{29}Si NMR spectra of Co_9S_8 (a) and Ni_3S_2 (b). The sharp peak at *ca.* -25 ppm is associated with residual silicone grease.

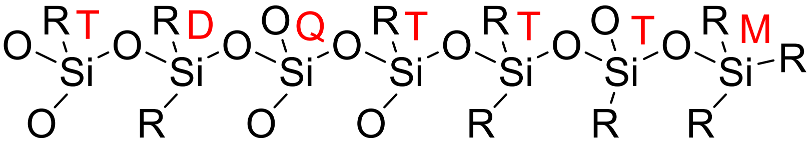

Figure S4. M, D, T and Q silicons in ^{29}Si NMR.

Table S2. Bond dissociation energies.	
Si-O	800 kJ / mol
Si-C	447 kJ / mol
C-H	338 kJ / mol

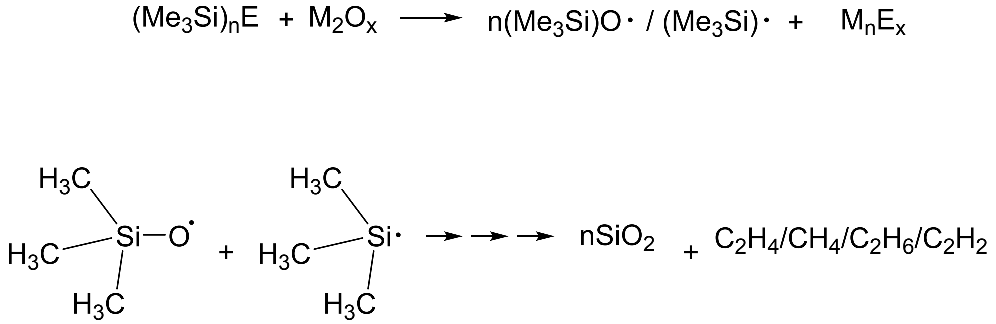

$$(Me_3Si)_nE + M_2O_x \longrightarrow n(Me_3Si)O\cdot / (Me_3Si)\cdot + M_nE_x$$

Scheme S1. Possible decomposition mechanism of excess trimethylsiyl reagents. See: A. Sonnenfeld, T. M. Tun, L. Zajickova, K. V. Kozlov, H.-E. Wagner, J. F. Behnke, R. Hippler, Plasmas and Polymers 6 (2002) 237.

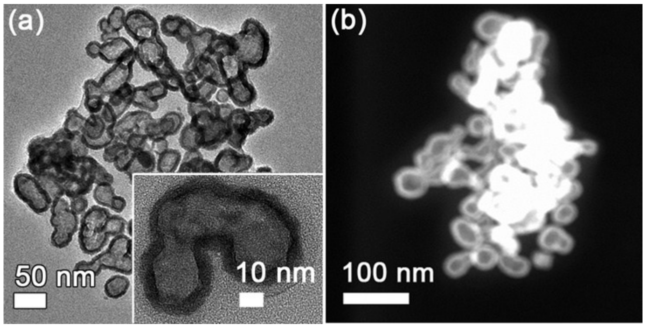

Figure S5. Representative bright field TEM (a) and HAADF-STEM (b) images of Ni_5Se_5 nanocrystals produced by silylative deoxygenation of NiO with TMS_2Se. Inset shows a magnified image of one hollow particle.

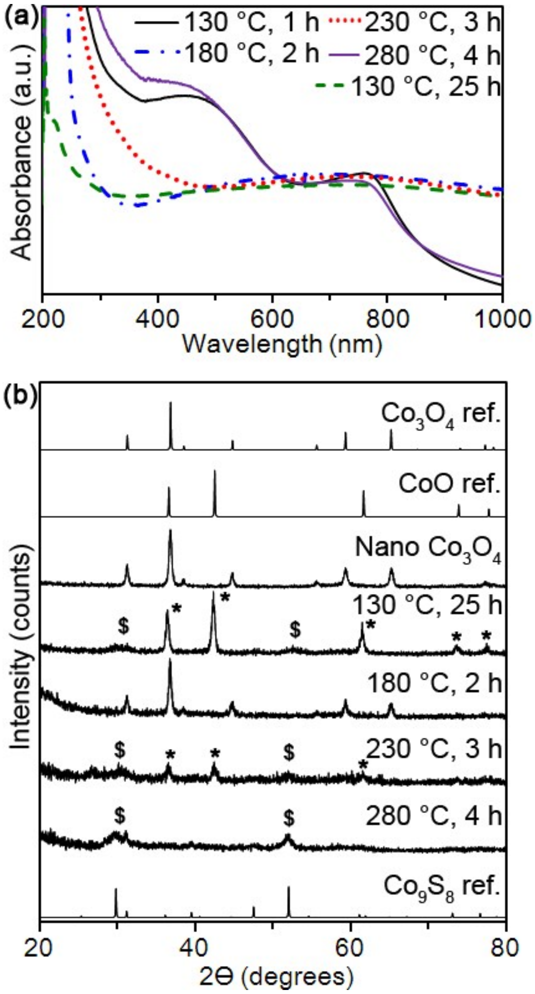

Figure S6. Solution-phase optical density spectra of aliquots during the reaction (a) and powder XRD data of Co_3O_4 nanocrystals, products the silylative deoxygenation of Co_3O_4 with TMS_2S and bulk references (b) (* = CoO, \$ = Co_9S_8).

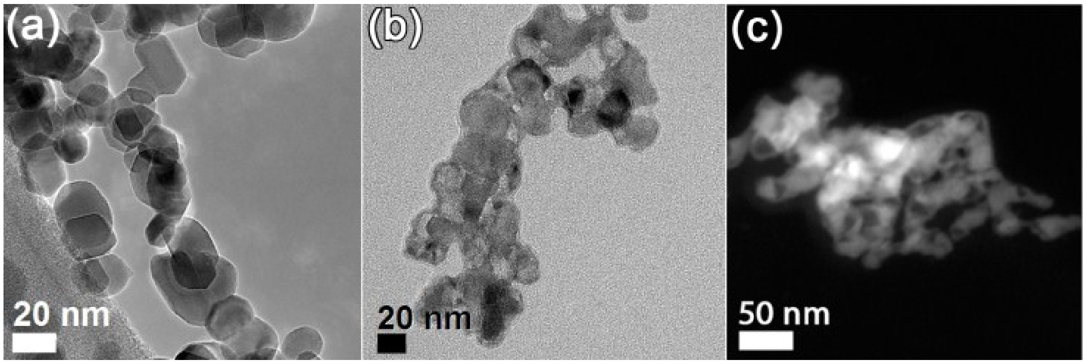

Figure S7. Representative TEM images of Co_3O_4 nanocrystals (a), bright field image (b) and HAADF-STEM image (c) of product after 25 h of silylative deoxygenation of Co_3O_4 with TMS_2S.

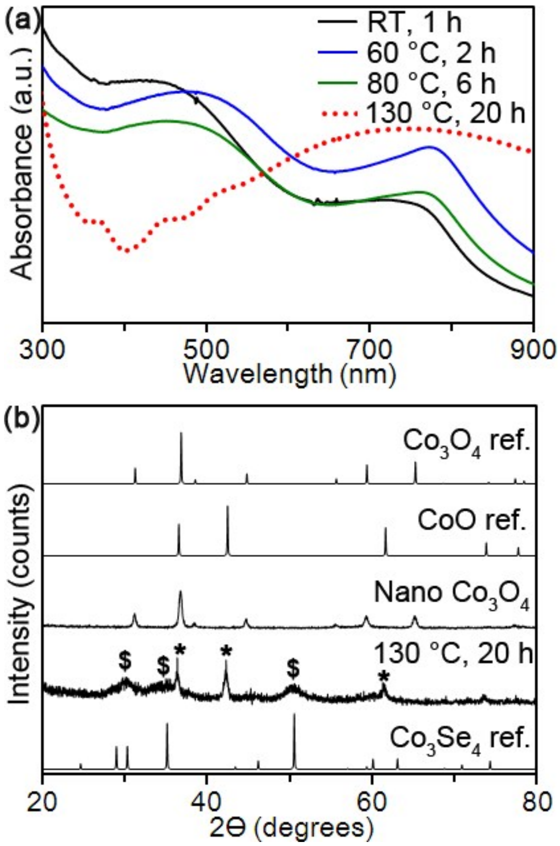

Figure S8. Solution-phase optical density spectra of aliquots during the silylative deoxygenation of Co_3O_4 with TMS_2Se reaction (a) and wide angle powder XRD data for Co_3O_4 nanocrystals, product after 20 h of reaction and bulk references (b) (* = CoO, $ = $MgAl_2O_4$ spinel-type Co_3Se_4).

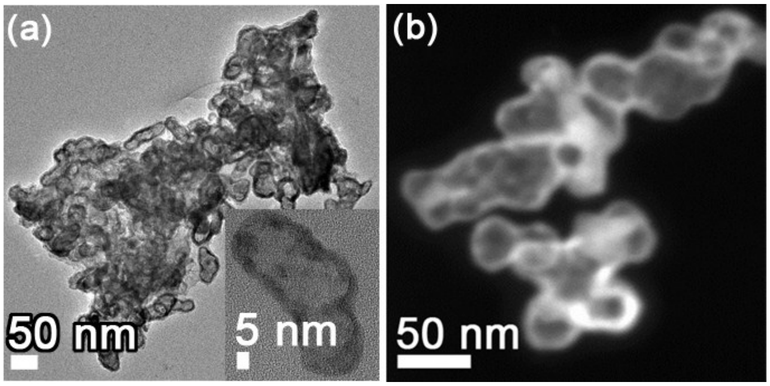

Figure S9. Representative TEM images of Co_3Se_4 nanocrystals after the silylative deoxygenation of Co_3O_4 with TMS_2Se; (a) shows a high magnification image of one particle with hollow morphology; (b) shows an HAADF-STEM image.

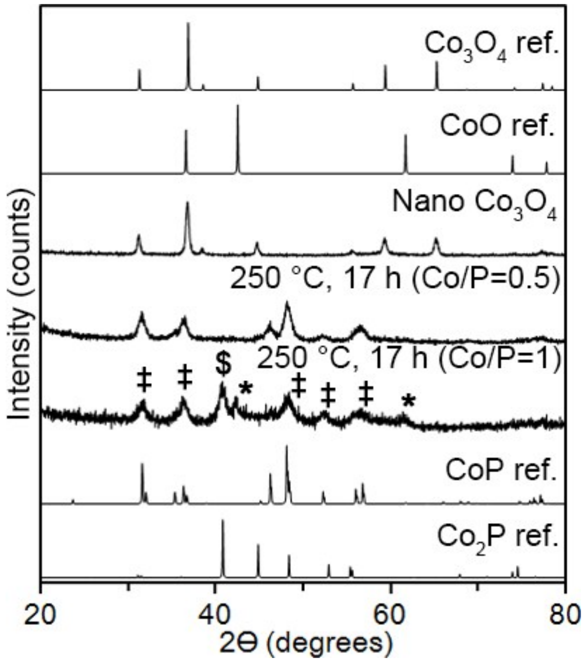

Figure S10. Powder XRD patterns of CoO nanocrystals and their silylative deoxygenation product upon reaction with TMS_3P. Reported XRD patterns for bulk rock salt CoO (*), MnP-type CoP (‡), and MnP-type Co_2P ($) are shown for comparison. Also shown is the synthetic Co/P ratio, determined by dividing three times the chemical amount (in moles) of Co_3O_4 over that of TMS_3P.

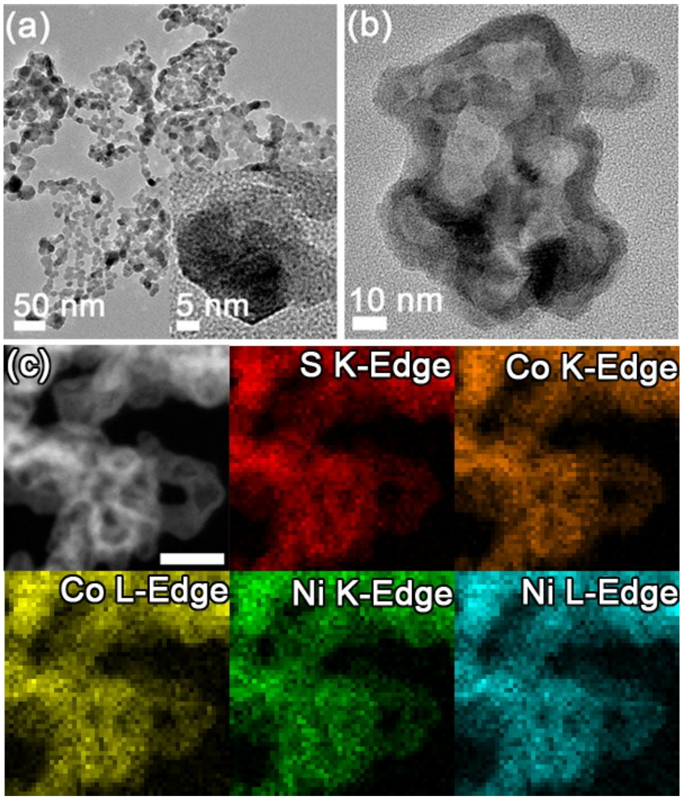

Figure S11. Representative TEM (a, b), and registered HAADF-STEM/EDS images (c) of $NiCo_2O_4$ nanocrystals (a) and the silylative deoxygenation product with TMS_2S (b, c). The scale bar in c corresponds to 50 nm.

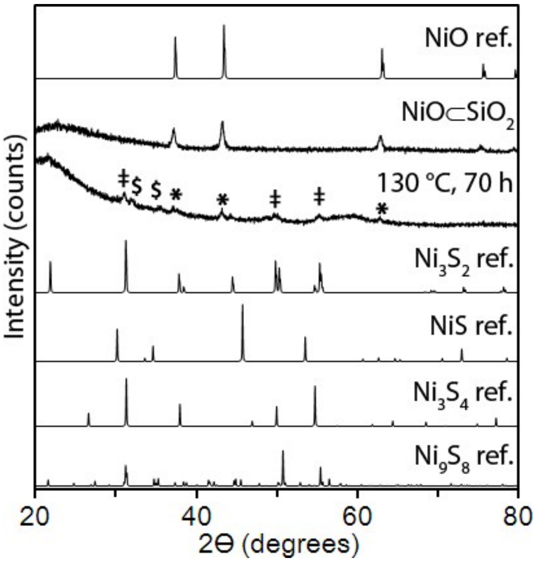

Figure S12. Powder XRD data for silylative deoxygenation of NiO$\subset$SiO$_2$ with TMS$_2$S, product and bulk references (* = NiO, ‡ = Ni$_3$S$_2$, \$ = Ni$_9$S$_8$).

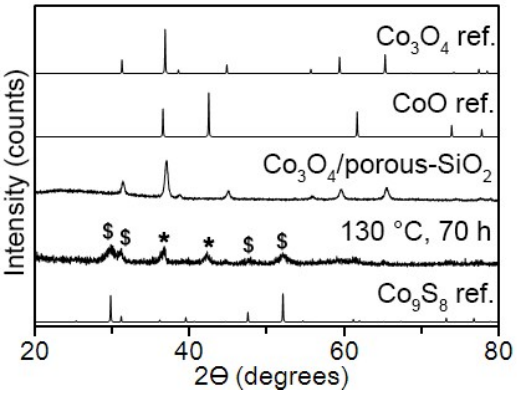

Figure S13. UV-Vis absorption spectra of aliquots during the silylative deoxygenation of Co$_3$O$_4$/porous-SiO$_2$ with TMS$_2$S (a) and powder XRD data for Co$_3$O$_4$/porous-SiO$_2$, product and bulk references (* = CoO, \$ = Co$_9$S$_8$).

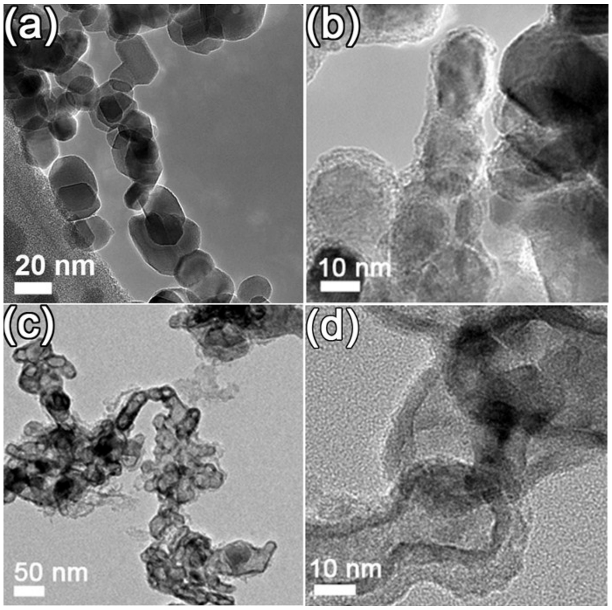

Figure S14. Representative TEM images of Co_3O_4 (a), Co_3O_4/porous-SiO_2 (3 nm-thick shell) (b), and its silylative deoxygenation product with TMS_2S, Co_9S_8/SiO_2 (c, d).

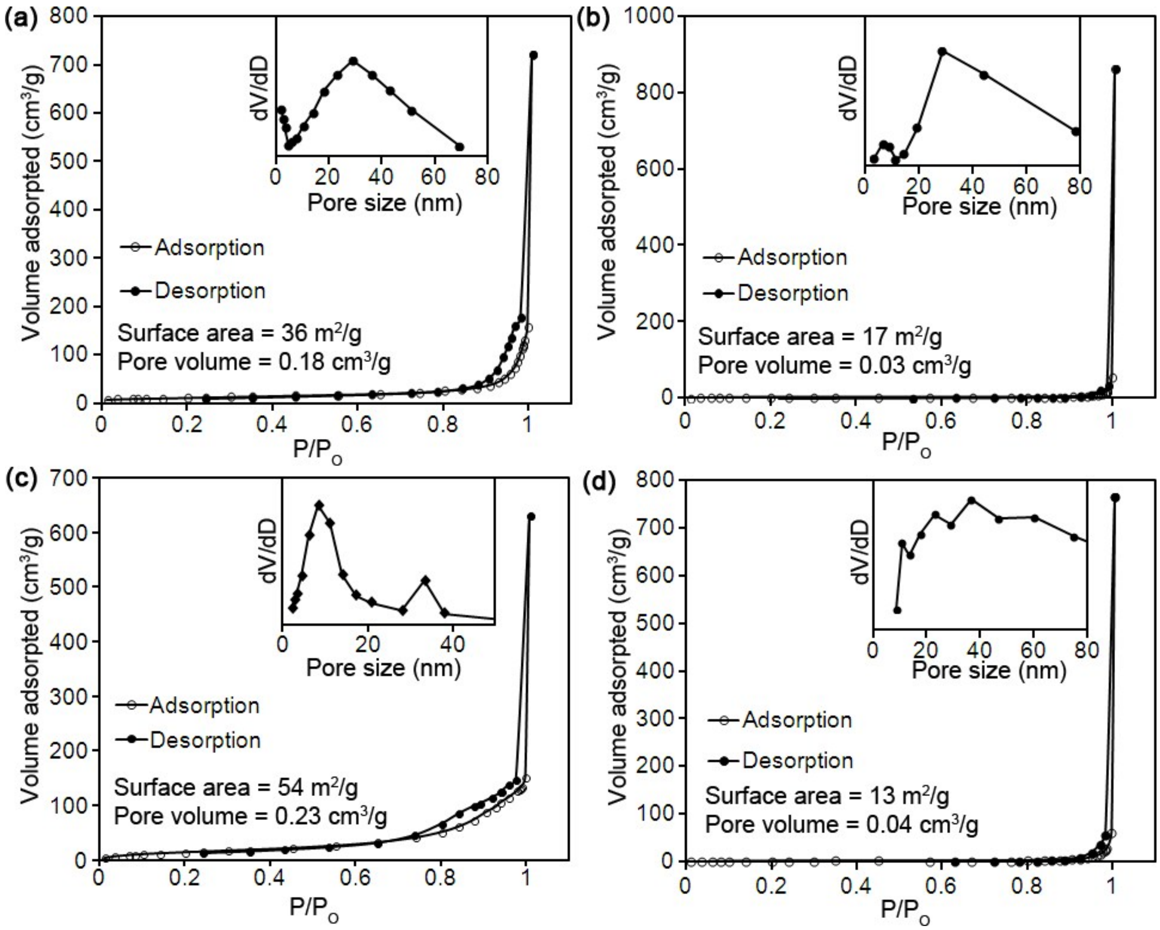

Figure S15. Nitrogen physisorption isotherms and BJH pore size distributions of NiO (a), Ni_3S_2 (b), CoO (c) and Co_9S_8 (d). The low surface area measurements indicate the resulting silica shells are not significantly porous. Introduction of a porous structure may require the use of a surfactant during the silylative deoxygenation process.